Journal of Materials Chemistry A

ROYAL SOCIETY OF CHEMISTRY

PAPER

View Article Online
View Journal | View Issue

Cite this: J. Mater. Chem. A, 2025, 13, 5961

MOF-derived nickel cobaltite: a pathway to enhanced supercapacitor performance†

Periyasamy Sivakumar, [a] Jayaraman Balamurugan,[b] C. Justin Raj,[c] Palaniappan Subramanian,[d] Antonysamy Dennyson Savariraj, [a] Ramu Manikandan[e] and Hyun Jung *[a]

Received 26th September 2024
Accepted 17th January 2025

DOI: 10.1039/d4ta06866a

rsc.li/materials-a

A streamlined design for nanoarchitecture can substantially enhance the performance of battery-type electrodes, leading to advanced hybrid supercapacitors (HSCs) with improved redox properties. Metal–organic frameworks (MOFs) are promising for electrochemical energy storage; however, they often suffer structural damage during calcination. We present a method to fabricate hierarchically layered sheet-like $NiCo_2O_4$ (NCO) nanostructures from MOFs. These nanostructures facilitate improved electron and ion transport while offering numerous electroactive sites. As supercapacitor electrodes, they exhibit a high specific capacity (~597 mA h g^{-1} at 1 A g^{-1}) and notable rate capability (69.2% retention). The NCO//AC HSC demonstrates a broad voltage window, a specific capacitance of ~152 F g^{-1} at 1 A g^{-1}, a high energy density (~47.3 W h kg^{-1} at ~908.2 W kg^{-1}), and excellent cycle stability (~90.8% retention after 10 000 cycles). This approach is both cost-effective and scalable for commercial energy storage applications.

1. Introduction

The rapid depletion of fossil fuels and environmental concerns have intensified the search for sustainable energy sources and advanced energy storage devices.[1] Supercapacitors (SCs) offer higher energy densities than traditional capacitors and greater power densities than batteries, but they often have low energy densities compared to rechargeable batteries.[2] To address this issue, hybrid supercapacitors (HSCs) combine capacitor-type and battery-type electrodes, enhancing energy and power capabilities.[3,4] The performance of HSCs depends on the structure and electrochemical properties of the electrode materials. Battery-type electrodes provide higher energy density and specific capacity due to effective redox charge transfer mechanisms.[5] Typical electrode materials should have a porous architecture, a large specific surface area, excellent electrical conductivity, and chemical stability.[6,7]

Developing advanced hierarchical nanoarchitecture materials with these properties is an advantage for high-performance HSCs and future energy storage technologies.[8,9] To enhance the performance of HSCs, significant efforts have focused on developing battery-type faradaic electrodes using transition metal oxides (TMOs) due to their high theoretical capacity and faradaic redox features. Binary TMOs (BTMOs) such as $CoMoO_4$ hollow-wire,[10] flower-shaped $Ni_3V_2O_8$,[11] $ZnCo_2O_4$ nanosheets,[12] interconnected CoV_2O_6,[13] $NiFe_2O_4$ nanoparticles,[14] and Fe_2VO_4 nanoparticles[15] are promising for their cost-effectiveness and eco-friendliness. Specifically, $NiCo_2O_4$ (NCO) shows superior electrochemical properties but tends to agglomerate during the electrochemical process, leading to an increase in the dead mass of the electroactive material.[16,17] The rational design of NCO with a porous architecture can enhance electron transport kinetics and prevent clustering. Sheet-like nanostructures with distinct porous features are particularly effective in improving performance by facilitating electrolyte penetration and ion diffusion.[18,19]

Metal–organic frameworks (MOFs) are promising for energy storage due to their tunable shape and porosity, large surface area, open metal sites, tailored composition, and ordered crystalline structure.[20,21] However, they suffer from structural disorder during the calcination process, which leads to a poor specific active surface area.[22,23] Most specifically, bimetallic MOFs are a type of MOF that consists of two different types of metal ions as nodes in the molecular structures, along with the

[a]Advanced Functional Nanohybrid Material Laboratory, Department of Chemistry, Dongguk University Seoul-Campus, Jung-gu, Seoul, 04620, Republic of Korea. E-mail: chemphile@dongguk.edu

[b]National Creative Research Initiative Center for Multi-Dimensional Directed Nanoscale Assembly, Department of Material Science and Engineering, Korea Advanced Institute of Science and Technology (KAIST), Daejeon, 34141, Republic of Korea

[c]Department of Physics, School of Advanced Sciences, Vellore Institute of Technology (VIT), Chennai Campus, Chennai – 600 127, Tamilnadu, India

[d]New Technologies – Research Center, University of West Bohemia, Plzeň 30100, Czech Republic

[e]Department of Energy and Materials Engineering, Dongguk, University Seoul-Campus, Jung-gu, Seoul, 04620, Republic of Korea

† Electronic supplementary information (ESI) available. See DOI: https://doi.org/10.1039/d4ta06866a

coordinating ligands, which provide increased redox-active metal centers and enhance structural stability, making them ideal for SC applications.[24,25] Optimizing the structural features of BTMO nanostructures derived from MOFs remains a key challenge.

We present an innovative and cost-effective synthesis of MOF-derived hierarchical layered nickel cobaltite (NCO) nanostructures with a distinctive porous architecture, utilizing a solvothermal method and followed by a controlled pyrolysis process. This method enables the rational design of highly effective electrode materials for high-performance HSCs. By precisely adjusting the solvothermal reaction temperature (STRT), we can fine-tune the morphological features and electrochemical properties of NCO nanostructures. The resulting NCO electrodes exhibit a hierarchical layered sheet-like nanoarchitecture, offering abundant electroactive sites that contribute to ultrahigh-specific capacity and excellent rate capability. Additionally, we engineered an HSC with optimal NCO nanostructures as the positive electrode and commercial activated carbon (AC; MSP20) as the negative electrode. This HSC demonstrates remarkable cycling stability, along with significantly enhanced energy and power densities, which underscores its potential for next-generation energy storage solutions.

2. Experimental section

2.1 Synthesis of MOF-derived NCO nanomaterials

The MOF-derived NCO nanomaterial was prepared using the following steps: (i) 1.5 mmol (0.436 g) of nickel(II) nitrate hexahydrate (Sigma-Aldrich) and 3.0 mmol (0.873 g) of cobalt(II) nitrate hexahydrate (Sigma-Aldrich) were dissolved in a solvent consisting of a mixture of double distilled water (15 ml) and ethanol (15 ml) (1 : 1 ratio) under magnetic stirring for 15 min. (ii) 3.0 mmol (0.498 g) of terephthalic acid (TA; Sigma-Aldrich) was dissolved in 50 ml of *N*,*N*-dimethylformamide (DMF; anhydrous 99.8%; Sigma-Aldrich) under stirring at room temperature for 15 min. (iii) The NiCo bimetallic nitrate solution was added gradually into the TA-DMF solution and stirred for 30 min. (iv) A 110 mL Teflon-lined stainless-steel autoclave was loaded with the reactant mixture and then heated at 175 °C for 12 h in a hot air oven. After this reaction, the supernatant was cleaned through repeated centrifugation using ethanol and dried under vacuum at 80 °C for 12 h. The acquired final product was pulverized into a fine powder and pyrolyzed at a rate of 5 °C min^{-1} to a temperature of 350 °C for 2 h in an ambient atmosphere. The resulting sample was designated as NCO-A. Furthermore, an analogous approach was utilized to prepare the samples at various STRTs such as 150, 125, and 100 °C, and the samples were labeled as NCO-B, NCO-C, and NCO-D, respectively.

The nickel-to-cobalt metal ratio was varied for comparative analysis at a total concentration of 4.5 mmol. The Ni^{2+} and Co^{2+} mixtures were prepared in two configurations: a 1 : 1 ratio (NCO-E) and a 2 : 1 ratio (NCO-F). These blends were subjected to STRT at 175 °C for 12 hours and then pyrolyzed at 350 °C for 2 hours in air.

Further details regarding the physicochemical characterization and electrochemical experiments can be found in the ESI.†

3. Results and discussion

The fabrication of the NCO-A nanomaterial follows a simple procedure. Initially, a solvothermal method is used to produce the base material. Subsequently, a pyrolyzing process, as illustrated in Fig. 1a, is employed to enhance the properties of the compound. Scanning electron microscopy (SEM) is one of the most prodigious tools for elucidating the surface morphology and microstructure of synthesized materials. The STRT is a crucial parameter in controlling the morphology of the nanomaterials. The morphological features of the obtained NCO materials under different STRT conditions were investigated using SEM analysis. The SEM images obviously reveal the detailed morphological topographies of the NCO materials. It is worth noting that the NCO-A material displays an intriguing surface morphology that is quite remarkable and easily discernible. This morphology takes the form of a highly intricate and delicate sheet-like nanoarchitecture, which is characterized by a hierarchical organization that is distributed throughout the entire structure. The architecture comprises numerous layers of nanosheets that are arranged precisely, resulting in a fascinating pattern. The structure also has void spaces in between, which further contribute to the unique and intriguing characteristics of the material, as illustrated in Fig. 1b and S1.† The thickness of the porous nanostructure consists of well-defined thin nanosheets of ~10–16 nm and lengths of a few micrometers. The porous architecture can be observed in the sheet-like nanostructure due to the pyrolysis process, which results in gaseous species being released from the base material. An apparent change in morphology was observed after lowering the STRT. Specifically, for the ~150 °C (NCO-B) material, the original hierarchical sheet-like nanostructure visibly transformed into a stacked sheet-like configuration. This alteration in the material's structure highlights the sensitivity of its synthesis conditions and the potential impact of subtle changes on the resulting material's properties. In addition, the stacked nanosheets have a thickness ranging from ~27 to 61 nm and a length of a few micrometers (Fig. S2a–c†). When the STRT is further decreased to a range of ~125–100 °C, there is a noticeable change in the structural appearance of the NCO materials. Modifications in the STRT cause significant alterations in the morphology of the materials. However, as the STRT decreased to ~125 °C (NCO-C), it began peeling off, transforming into an irregular plate-like structure. The NCO-C irregular plates showed a thickness of ~87–147 nm and a length of a few micrometers (Fig. S2d–f†). At an STRT of ~100 °C, an apparent change was observed in the NCO-D morphology. The transformation was observed to resemble a thick block-like structure, suggesting the possibility of a change in its physical properties. This structure is distinct and can be clearly distinguished from other morphologies observed at different STRTs. The SEM images of the NCO-D sample show that the block has a thickness of ~726–938 nm and a length of a few micrometers, as presented in Fig. S2g–i.† It is worth

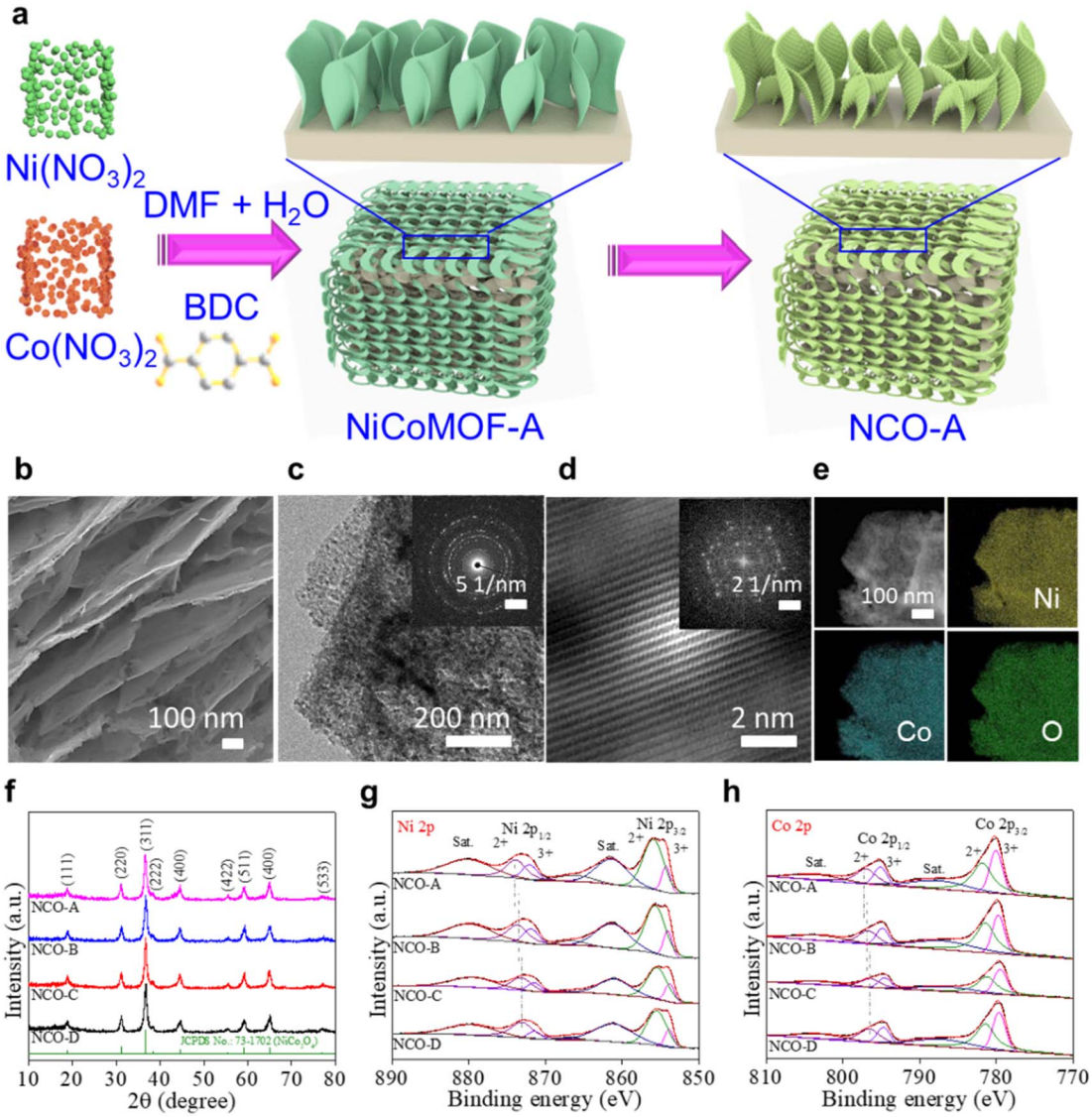

Fig. 1 (a) Schematic representation for the design of the layered sheet-like NCO-A nanoarchitecture, (b) SEM, (c) TEM (the inset shows the SAED pattern), (d) HR-TEM (the inset shows the FFT pattern), (e) STEM patterns with the corresponding EDS mapping of Ni, Co, and O of the hierarchical sheet-like NCO-A nanoarchitecture, (f) XRD patterns, (g) Ni 2p XPS, and (h) Co 2p XPS of NCO-A, NCO-B, NCO-C, and NCO-D nanomaterials.

noting that the physical structure and form of the NCO materials remained unaltered even after pyrolyzing at ~350 °C, indicating its structural stability. This present investigation reveals that the NCO materials preserve their morphology and are thermally stable in an ambient atmosphere. In addition, the surface morphology of the NCO materials was slightly altered after the calcination process compared to the NiCoMOFs (Fig. S3†). After undergoing thermal treatment, the surface of the NCO materials exhibits a rougher morphology compared to NiCoMOFs. This roughness can be attributed to the evolution of gaseous species that occur during the thermal treatment process. Furthermore, the SEM images presented in Fig. S2(j–o)† depict the structural characteristics of the materials synthesized at various nickel (Ni) to cobalt (Co) ratios at a specific STRT of 175 °C, specifically for samples designated as NCO-E and NCO-F. Notably, these images illustrate a complete collapse of the intended sheet-like architecture that was expected from the synthesis process. This structural failure can be attributed to the variations in Ni to Co ratios utilized during the preparation. It appears that these variations led to moderate aggregation of the material rather than resulting in the formation of larger crystalline structures. This outcome suggests that the chosen ratios may have played a critical role in influencing the overall morphology and stability of the materials produced.

The detailed structural and morphological characteristics of the synthesized NCO-A, NCO-B, NCO-C, and NCO-D were further investigated by TEM, HRTEM, SAED, and EDS elemental mapping. Fig. 1c and S4a† exhibit low- and high-magnification TEM images of the hierarchical sheet-like NCO-A nanoarchitecture. The TEM analysis clearly reveals a hierarchical sheet-like nanoarchitecture with a porous network that is composed of a plentiful number of nanoparticles with

a diameter of ~2.9–4.4 nm. Meanwhile, the nanoparticles are interconnected with each other to form a highly porous architecture, which provides more electroactive sites to improve the ion/electron transport kinetics. Fig. S5a and b† clearly show that the thick sheet-like NCO-B nanostructures are packed and associated with adjacent nanosheets containing a variety of internal nanoparticles having diameters in the range of ~5.0–7.2 nm. Moreover, the TEM images of the NCO-C nanomaterial reveal that the crumpled sheet is filled with many nanoparticles with an average diameter of ~5.8–9.1 nm, as seen in Fig. S6a and b.† However, the TEM image of the NCO-D nanomaterial displays a compressed block-like structure filled with numerous nanoparticles, with a diameter of ~9.4–12.6 nm, as presented in Fig. S7a and b.† Additionally, it can be observed that when the STRT increases, the particle size decreases, the inter-particle distance decreases, the particles are packed much closer, and consequently, the roughness decreases. The corresponding SAED patterns (inset of Fig. 1c, S5b, S6b and S7b†) reveal spotty rings, which further confirm the polycrystalline characteristics of the NCO-A, NCO-B, NCO-C, and NCO-D nanomaterials. The HRTEM image of the NCO-A, NCO-B, NCO-C, and NCO-D nanomaterials further confirms the highly crystalline characteristics (Fig. 1d, S4b, S5c, S6c and S7c†). The noticeable interplanar fringes display an interplanar spacing of ~0.24 nm, corresponding to the (311) planes of the $NiCo_2O_4$ crystalline structure (JCPDs #: 73-1702). The elemental distributions of the NCO-A, NCO-B, NCO-C, and NCO-D nanostructures were further investigated using scanning TEM (STEM) EDX studies, and the results are presented in Fig. 1e, S5d, S6d and S7d.† The STEM-EDX analysis clearly demonstrated that nickel (Ni), cobalt (Co), and oxygen (O) are homogenously distributed throughout the NCO nanostructures.

The powder XRD measurements were employed to examine the structural characteristics of the prepared nanomaterials. Fig. 1f and S8c† display the XRD patterns of the NCO-A, NCO-B, NCO-C, NCO-D, NCO-E, and NCO-F nanomaterials. All the diffraction peaks that are detected in the NCO materials correspond to the $NiCo_2O_4$ crystalline phase (JCPDS no.: 73-1702). The $NiCo_2O_4$ compound possesses a cubic spinel structure consisting of binary metal oxides. Within this structure, octahedral sites are occupied by all nickel ions, while cobalt ions are distributed among both tetrahedral and octahedral sites.[26] Furthermore, the observed additional peaks in the XRD patterns of the NCO-E and NCO-F nanomaterials are attributed to the crystalline structure of NiO (JCPDS no.: 44-1159). This finding suggests that, alongside the dominant NCO phase, there is a significant formation of the NiO phase. The results indicate that as the concentration of nickel in the metal precursors increases, there is a corresponding enhancement in the formation of the highly crystalline NiO phase. This phenomenon highlights the relationship between precursor composition and the resulting structural characteristics of the synthesized nanomaterials, demonstrating how variations in the Ni/Co metal concentration can influence phase development and crystallinity. Besides, the experimental findings indicate that the pristine NiCoMOF crystals undergo decomposition upon calcination (Fig. S8(a and b)†). This observation is distinct from the behavior of NCO nanomaterials, which exhibit different crystal structures, suggesting that the pyrolysis process induces significant changes in the crystal structure and composition of NiCoMOFs. Furthermore, the impact of the STRT on crystallite size is evident from the results. The crystallite size increases from 11 to 14 nm as the STRT decreases from 175 °C to 100 °C. The change in crystal size may be attributed to a change in the crystal structure of the metal-MOF. With an increase in the STRT, the surface area is likely to expand owing to the growth and construction of intergranular linkages. Besides, this could probably be a change in the crystal size due to a change in the crystal structure of the metal-MOF. Subsequently, the surface energy is expected to decrease. As a consequence of the movement of grain boundaries, the particles tend to clump together, leading to the formation of voids. This process ultimately results in a reduction of the material's porosity, thereby altering its physical structure.[27]

The elemental compositions and valence states of the NCO electrode materials were analyzed using the XPS technique. The full scan XPS spectra of the NCO-A, NCO-B, NCO-C, and NCO-D nanomaterials are presented in Fig. S9a.† The XPS analysis of the NCO nanomaterials indicates the presence of Ni 2p, Co 2p, and O 1s species in the survey spectrum. Fig. 1g illustrates the Ni 2p spectra, which exhibit two distinct peaks at ~855.5 eV and ~873.1 eV. These peaks are commonly attributed to Ni^{2+} ions. Additionally, two other peaks at ~853.9 and ~871.4 eV are observed, indicative of Ni^{3+} ions, consistent with earlier reports.[28] Besides, satellite peaks were observed at ~861.1, ~866.9, and ~879.7 eV, corresponding to the binding energies of Ni $2p_{3/2}$ and Ni $2p_{1/2}$, respectively. Moreover, the deconvoluted Co 2p spectra are presented in Fig. 1h. The Co $2p_{3/2}$ and Co $2p_{1/2}$ emission spectra were analyzed and exhibited two distinct spin–orbit peak features associated with Co^{2+} and Co^{3+}. In particular, the high-resolution Co $2p_{3/2}$ spectrum reveals two distinct peaks. The first peak is situated at ~779.6 eV, indicating the presence of Co^{3+}. The second peak, located at ~781.4 eV, clearly indicates the presence of Co^{2+}. The Co $2p_{1/2}$ high-resolution spectra exhibit a discernible peak at ~794.7 eV, indicative of Co^{3+}, and another peak at ~796.6 eV, which is characteristic of Co^{2+}. Additionally, satellite peaks are observed at ~786.9 eV and ~802.9 eV, which are associated with the binding energies of Co $2p_{3/2}$ and Co $2p_{1/2}$, respectively. The above findings agree well with the earlier reports.[10] Importantly, when STRT is raised, a slight red shift can be observed in the Ni 2p and Co 2p spectra of the NCO-A and NCO-B nanomaterials, compared to the NCO-C and NCO-D nanomaterials. It can be ascribed to the volume expansion of the crystal lattice because of the formation of the hierarchical thin sheet-like nanoarchitecture.[29] The core-level O 1s spectra found on the surface can be effectively fitted with approximately three peaks located at ~529.3, ~531.1, and ~532.3 eV, respectively, as presented in Fig. S9b.† The O_a peak observed at ~529.3 eV can be ascribed to metal–oxygen chemical bonds, which strongly indicate the existence of Ni–Co–O. Meanwhile, the O_b peak detected at ~531.1 eV could be associated with defect/vacancy sites with low oxygen coordination. The O_c peak centered at ~532.3 eV is generally attributed to the presence of physically/chemically

adsorbed H_2O molecules on the surface of NCO.[30,31] The area proportion of O_a/O_b reflects the oxygen vacancy on the surface of the metal oxide lattice, which is closely associated with enhanced electrochemical activity.[32] The area proportion of O_a/O_b is ~1.82, ~1.61, ~1.43, and ~1.16 for NCO-A, NCO-B, NCO-C, and NCO-D nanomaterials, respectively. This is owing to the use of oxygen by carbon in the form of CO_2 in the NCO system derived from the NiCoMOF structure through air oxidation, which causes disruption in the lattice, and the resulting oxide exhibits oxygen vacancies.[31]

It is widely recognized that incorporating active electrode materials with a significantly high specific surface area and a distinctive porous architecture can lead to an increase in the electroactive sites and thereby enhance the electrochemical performance of SCs. The porous structures of the prepared NCO-A, NCO-B, NCO-C, and NCO-D nanomaterials were investigated by employing N_2 sorption isotherm analysis. All the NCO nanomaterials are found to exhibit a type-IV isotherm with an H3-model hysteresis loop under the applied relative pressure, as observed in the N_2 desorption isotherm study (Fig. S9c†), demonstrating the existence of mesoporous architectures of the synthesized electrode materials. The well-defined sheet-like NCO-A nanoarchitecture exhibits a high BET specific surface area of ~63 $m^2\ g^{-1}$, which is comparatively higher than those of other electrode materials such as NCO-B, NCO-C, and NCO-D, which have surface areas of ~52, ~47, and ~38 $m^2\ g^{-1}$, respectively. The process of redox reactions mimicking storage tends to occur predominantly on the surface or in close proximity to the materials found within electrodes. A greater specific surface area would result in an increased number of active reaction sites available for the occurrence of faradaic reactions, thus leading to superior electrochemical performance. The distribution of pore sizes in the NCO nanomaterials was analyzed using the Barrett–Joyner–Halenda (BJH) technique, and the results are presented in Fig. S9d.† The well-defined sheet-like NCO-A nanoarchitecture has a mean pore diameter of ~19.18 nm, signifying its mesoporous characteristics. In addition, the NCO-B, NCO-C, and NCO-D nanomaterials display a mean pore diameter of ~21.20, ~22.46, and ~24.22 nm, respectively. In addition, the four NCO nanomaterials, namely NCO-A, NCO-B, NCO-C, and NCO-D, exhibit total pore volumes of ~0.286, ~0.265, ~0.249 $cm^3\ g^{-1}$, and ~0.231 $cm^3\ g^{-1}$, respectively. The resultant N_2 sorption/desorption isotherm analysis demonstrated that the sheet-like NCO-A nanoarchitecture obtained has a significantly higher specific surface area and appropriate pore characteristics compared to other NCO nanomaterials. The huge pore volume and narrow pore features are unique to this material, creating a pathway for the electrolyte ions to diffuse rapidly toward the electrode. This, in turn, accelerates the electrochemical redox reaction.[33,34] The porous sheet-like structure of the NCO-A nanoarchitecture provides a significant amount of void space, resulting in a large specific surface area and significantly improving the electrode material's charge storage capacity.[33]

To achieve higher-performance SCs, it is crucial to tackle a range of challenges, with particular emphasis on ensuring that the electrode and electrolyte are compatible. The degree to which an electrode surface can be wetted is essential when assessing its surface energy and enabling charge transportation at the electrode/electrolyte interface.[35] To evaluate the interaction between the electrode surfaces and the electrolyte, it is essential to measure the contact angle, as it offers valuable information about the hydrophilicity and fruitful surface energy of the electrodes.[36] There is an obvious inverse relationship between surface free energy and the contact angle. The contact angles of the pristine NF, NCO-A, NCO-B, NCO-C, and NCO-D electrodes in a 6 M KOH electrolyte, as shown in Fig. 2a–e, are estimated to be 0°, 70°, 81°, 100°, and 110°, respectively. The NCO-A electrode has the smallest contact angle, demonstrating its high wettability and surface energy.[37] This indicates the potential for enhanced electrochemical performance of the NCO-A electrode in comparison to other electrodes. The 3rd-order polynomial expression was applied to quantitatively evaluate the surface energy (SE; mJ m^{-2}) of the electrode materials, which is expressed as follows:[38]

$$\mathrm{SE} = X(\theta)^3 - Y(\theta)^2 - Z(\theta) + \gamma_L \quad (1)$$

where X, Y, and Z represent unique constants for each liquid, θ is the contact angle in radians, and γ_L represents the surface tension of the liquid in mJ m^{-2}. In a series of experiments, four distinct liquids, each possessing identified surface tension characteristics, were employed (Fig. 2f). These liquids, including DIW, glycerol, formaldehyde, and ethylene glycol, served as benchmarks to evaluate surface energy by utilizing contact angles.[37,38] The estimated surface free energies for NCO-D, NCO-C, NCO-B, and NCO-A electrodes are 17.92, 23.34, 34.69, and 41.52 mJ m^{-2}, respectively, as displayed in Fig. 2g. The exceptional surface energy results from the highly delicate sheet-like nanoarchitecture of the NCO-A electrode material. This nanoarchitecture is characterized by a hierarchical arrangement that spans the entire structure. Additionally, the structure contains void spaces that contribute to the distinct and fascinating properties of the material. The angle at which a liquid meets a surface is affected by the surface energy. This angle increases on surfaces with low energy and decreases on surfaces with high energy due to the surface roughness.[36,39] The NCO-A electrode exhibits a diminished contact angle and elevated surface energy compared to its counterparts, resulting in improved charge transfer efficiency and optimal utilization of electrode materials.

A comprehensive investigation was conducted to examine the electrochemical properties of the NCO electrodes for achieving optimal performance and adaptability for SC applications. CV and GCD studies were performed to gain further insight into the relationship between the STRT and the electrochemical properties of the NCO electrode materials. The electrochemical studies show that the material prepared at an STRT of ~175 °C exhibits better electrochemical behavior than the electrode materials prepared at STRTs of ~100, ~125, and ~150 °C. This is mainly due to the excellent morphological and textural properties of the nanomaterial, which can lead to faster kinetics of electron and ion transport. The CVs of NCO-A, NCO-B, NCO-C, NCO-D, NCO-E, and NCO-F are obtained using a 3-

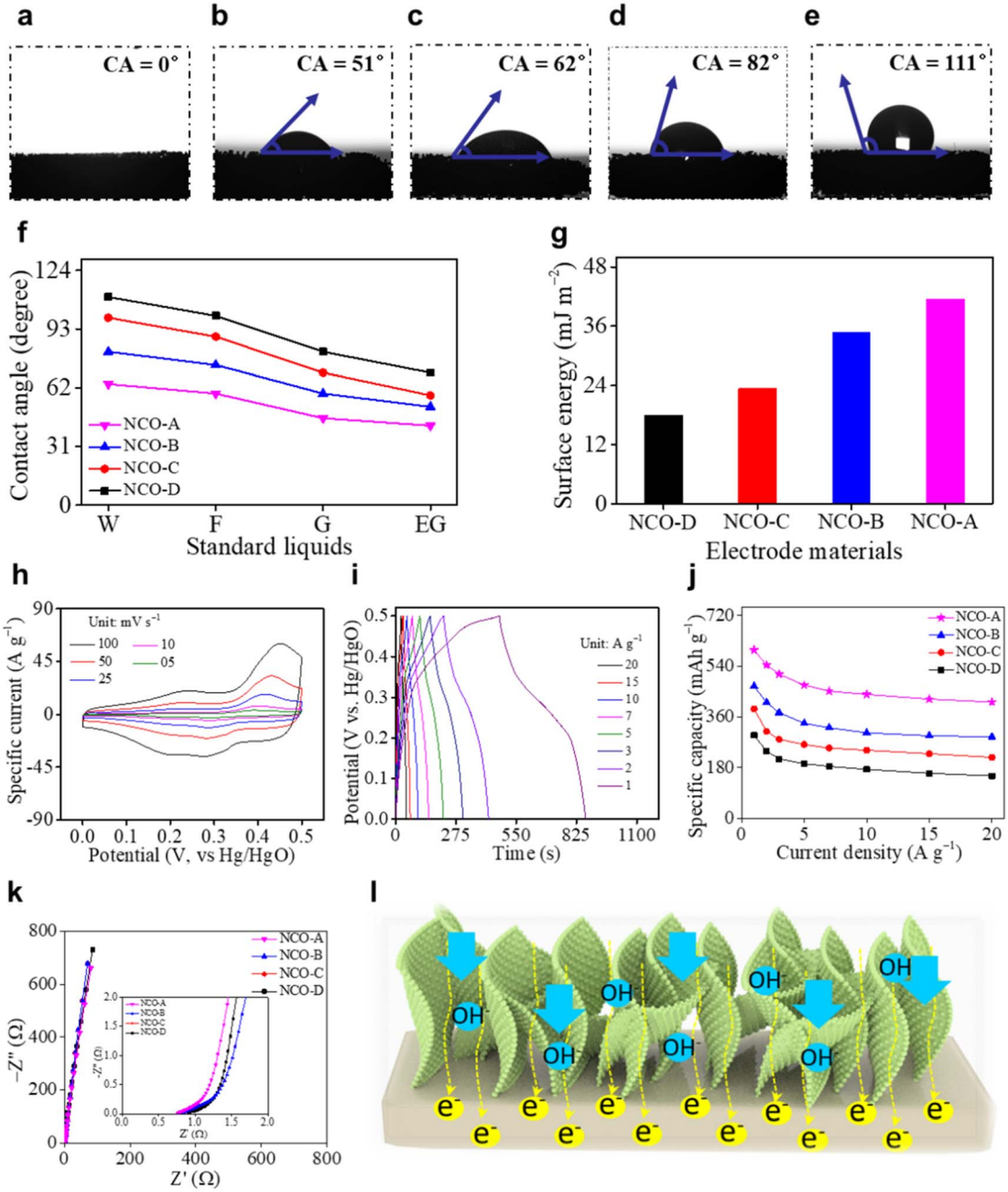

Fig. 2 Contact angle measurements of (a) bare NF, (b) NCO-A, (c) NCO-B, (d) NCO-C, and (e) NCO-D electrodes with 6 M KOH solution, (f) contact angle of NCO-A, NCO-B, NCO-C, and NCO-D electrodes with DI-H_2O (W), formamide (F), glycerol (G), and ethylene glycol (EG) standard liquids, (g) surface energy of NCO-A, NCO-B, NCO-C, and NCO-D electrodes, (h) CVs at various sweep rates of the NCO-A electrode, (i) GCD plots at various currents of the NCO-A electrode, (j) resulting capacity as a function of the different current densities of NCO-A, NCO-B, NCO-C, and NCO-D electrodes, (k) EIS plots of NCO-A, NCO-B, NCO-C, and NCO-D electrodes, and (l) a schematic diagram illustrating the benefits of the NCO-A layered nanosheet electrode in the energy storage process.

electrode system in a 6 M KOH aqueous electrolyte at a constant scan rate of 25 mV s^{-1}, as exhibited in Fig. S10a.† The obtained CVs of the samples exhibit distinctive characteristics compared to conventional electric double-layer capacitors (EDLCs), indicating that the hierarchical sheet-like NCO-A nanostructure electrode exhibits faradaic behavior resembling that of a battery-type electrode material. The proposed mechanism for storing electrochemical energy is outlined below:[40]

$$NiCo_2O_4 + OH^- + H_2O \leftrightarrow NiOOH + 2CoOOH + e^- \quad (2)$$

$$CoOOH + OH^- \leftrightarrow CoO_2 + H_2O + e^- \quad (3)$$

Among the NCO-A, NCO-B, NCO-C, NCO-D, NCO-E, and NCO-F electrode materials, the CV area of the hierarchical sheet-like NCO-A nanostructure electrode is impressively larger. The results indicate that the NCO-A nanostructure exhibits

superior electrochemical properties with increased energy storage even at the same scan rate. The superior performance of the NCO-A nanostructure electrode can be attributed to its hierarchical layered sheet-like nanostructure characteristics. This structure not only facilitates the smooth flow of electrons but also ensures efficient ion transfer, thereby improving the overall performance of the electrode.[41] Consequently, it is easy to deduce that the hierarchical NCO-A nanostructure is the ideal electrode material based on an evaluation of its distinct sheet-like porous architecture and electrochemical performance. Fig. S11a† displays the GCD profiles of the NCO-A, NCO-B, NCO-C, NCO-D, NCO-E, and NCO-F electrodes at a constant current density of 1 A g^{-1}. The hierarchical NCO-A nanostructure electrode demonstrated remarkable performance in terms of GCD time, surpassing the capacity performance of NCO-B, NCO-C, NCO-D, NCO-E, and NCO-F electrodes. The results are consistent with the CV findings. Besides, it has been verified that the electrodes exhibit non-linear GCD profiles, which confirms the battery-type faradaic characteristics. The remarkable electrochemical characteristics of the hierarchical NCO-A nanostructure electrode can be attributed to its exceptional properties, such as its layered sheet-like morphology with a hierarchical structure, high specific surface area, and excellent conductivity.[42]

The CVs measured at different scan rates ranging from 5 to 100 mV s^{-1} for the hierarchical sheet-like NCO-A nanostructure electrode are presented in Fig. 2h. The CVs exhibit distinct redox peaks that are indicative of the battery-type faradaic reactions. The capacity properties are mainly influenced by the faradaic redox reactions. This observation is noteworthy because EDLCs typically exhibit a CV curve resembling a perfect rectangular shape. The faradaic reactions are reflected in the anodic and cathodic peaks, which are observed at approximately 0.41 V and 0.28 V, respectively. These observations indicate the reversible nature of the hierarchical NCO-A nanostructure electrode. Besides, ramping up the scan rates notably affects the oxidation and reduction peaks. Specifically, the slight peak shifts to the positive and negative directions, respectively, are linked to the internal resistance of the electrode materials. In addition, the observed increase in peak current as the scan rate increases indicates that the electronic and ionic transport rates are rapid enough at the given potentials. Furthermore, the CVs display a significant increase in area as the scan rate increases from 5 to 100 mV s^{-1}. This phenomenon suggests that the electrode materials possess exceptional rate capability, as the shape of the peaks is maintained even at high scan rates.[43] For comparison, the CVs of NCO-B, NCO-C, NCO-D, NCO-E, and NCO-F electrodes at various scan rates were also plotted and are shown in Fig. S10b–f.†

Fig. 2i displays the GCD profiles of the NCO-A electrode at various current densities. For comparison, the GCD curves of NCO-B, NCO-C, NCO-D, NCO-E, and NCO-F electrodes are presented in Fig. S11c–g.† The GCD profiles exhibited remarkable faradaic redox characteristics with evident charging and discharging plateaus, which corresponded well with the CV analyses. The GCD profiles of the hierarchical NCO-A nanostructure electrode exhibit a pronounced symmetrical and non-linear shape, which confirms the exceptional electrochemical properties of the material. Additionally, it suggests that the material possesses impressive reversible redox kinetics. Moreover, the GCD profiles show no significant IR drop, indicating excellent rate capability and coulombic efficiency of the hierarchical NCO-A nanostructure electrode. The GCD profiles are in accordance with the CV investigation.

The specific capacity based on the integral area under the discharge profile of GCD curves is presented in Fig. 2j and S11b.† The hierarchical NCO-A nanostructure electrode exhibited high specific capacity ranging from ~597 to 413 mA h g^{-1} at various current densities (1 to 20 A g^{-1}). The trend observed in the specific capacity shows a gradual decrease with an increase in current density. This phenomenon can be attributed to the reduced effectiveness of the active material in the electrochemical system at high current densities. Furthermore, the specific capacities of the NCO-B, NCO-C, NCO-D, NCO-E, and NCO-F electrodes are approximately 469, 389, 295, 557, and 522 mA h g^{-1}, respectively, at a current density of 1 A g^{-1}. These values are significantly lower than the specific capacity of the NCO-A electrode. Specifically, the hierarchical NCO-A nanostructure electrode retained 69.2% of its capacity, whereas NCO-B, NCO-C, NCO-D, NCO-E, and NCO-F electrodes retained 61.6%, 55.6%, 50.9%, 65.1%, and 63.3%, respectively. The impressive rate capability of the hierarchical sheet-like NCO-A nanostructure electrode is evident in comparison to the NCO-B, NCO-C, NCO-D, NCO-E, and NCO-F electrodes, as demonstrated by these results. The exceptional rate performance can be attributed to the efficient transport of ions and enhanced electronic conductivity,[44] further supported by electrochemical impedance spectroscopy (EIS) analysis.

The fast rate capability of the electrode material is attributed to its efficient ion-transport kinetics and enhanced electronic conductivity, as verified through EIS. The Nyquist plots of the NCO-A, NCO-B, NCO-C, and NCO-D electrodes are shown in Fig. 2k. The impedance plots obtained from all electrodes exhibit a suppressed semicircle at high frequencies, which is attributed to the charge transfer resistance (R_{ct}) of the active electrode materials. On the other hand, the almost linear response observed at low frequencies is indicative of the redox behavior of the electrodes in an aqueous KOH electrolyte. The point at which the high-frequency region intersects with the Z'-axis provides information about the internal resistance (R_s). This resistance is determined by factors such as the electrolyte ionic resistance, the intrinsic resistance of the substrate, and the contact resistance at the interface of the active material and the current collector. At lower frequencies, the hierarchical NCO-A nanostructure electrode exhibits a steeper slope in the straight line region compared to the NCO-B, NCO-C, NCO-D, NCO-E, and NCO-F electrodes. This indicates that the hierarchical NCO-A nanostructure electrode has lower diffusive resistance, which facilitates the diffusion of ions and improves the transport kinetics within the electrode materials. Furthermore, the Nyquist plots were modeled with an appropriate equivalent circuit, as shown in Fig. S13,† and the obtained fit parameters are listed in Fig. S14 and Table ST1.† The equivalent circuit consists of a series resistance representing the solution

resistance (R_s), and R_{ct} is the charge transfer resistance, corresponding to the suppressed semicircle at high frequencies. Besides, the slightly tilted low-frequency slope in the plot is assigned to the ion diffusion resistance (R_w). Furthermore, a constant-phase element (CPE) and a capacitor (C_p) were added to the circuit, which explains the energy storage process resulting from the EDLC and redox process in the electrode. Noticeably, the hierarchical NCO-A nanostructure electrode has a significantly lower R_s of ~0.7087 Ω as compared to NCO-B (~0.7643 Ω), NCO-C (~0.8435 Ω), NCO-D (~0.8873 Ω), NCO-E (~0.7268 Ω), and NCO-F (~0.7394 Ω) electrodes. This indicates that the hierarchical NCO-A nanostructure electrode has lower intrinsic resistance than the other NCO electrodes. The EIS results clearly show that the R_{ct} value of the hierarchical NCO-A nanostructure electrode is ~0.5267 Ω, which is lower than the R_{ct} values of NCO-B (~0.8083 Ω), NCO-C (~0.8377 Ω), and NCO-D (~0.8789 Ω), NCO-E (~0.6136 Ω), and NCO-F (~0.7275 Ω) electrodes. The results obtained from EIS are in complete agreement with the curves obtained from CV and GCD profiles. The hierarchical NCO-A nanostructure electrode demonstrates extremely low internal resistance, which results in enhanced charge transport kinetics and an improved redox reaction process. The observed phenomenon can be ascribed to the well-structured layered sheet-like morphology with porous features and a high surface area of the hierarchical NCO-A nanostructure architecture. These characteristics are believed to facilitate the diffusion of electrolytes through the accessible active channels present in the layered sheet-like nanoarchitecture. This, in turn, leads to a substantial enhancement in its performance in electrochemical processes, as illustrated in Fig. 2l.

Fig. S11h and i† present a comprehensive analysis of the cyclic stability profiles for NCO electrodes subjected to a current density of 10 A g^{-1} over 5000 continuous GCD cycles. The results indicate that the NCO-A electrode exhibits remarkable performance, retaining 94% of its capacity after the full cycling period. In comparison, the NCO-B electrode demonstrates a lower retention rate of 89%, while the NCO-C and NCO-D electrodes exhibit even less stability, retaining only 88% and 86% of their capacitance, respectively. The NCO-E and NCO-F electrodes show similar performances, with capacity retentions of 92% and 90%, respectively. These findings highlight the superior structural integrity and cyclic durability of the NCO-A electrodes, confirming their exceptional capacity for maintaining performance over prolonged cycling periods when compared to the other tested variants. As illustrated in Fig. S12a–f,† the NCO-A electrode demonstrates remarkable stability by retaining its original shape even after undergoing a series of electrochemical measurements. This stands in stark contrast to the behavior observed in other NCO electrodes, which tend to undergo noticeable morphological changes. The sustained structural integrity of the NCO-A electrode contributes significantly to its performance, indicating a strong association between the active phase of NCO-A and its morphological stability. These combined attributes not only validate the robustness of NCO-A but also highlight the synergetic effect that arises from this integration, ultimately leading to superior electrochemical performance when used as a battery-type electrode. The findings affirm that the unique combination of stable morphology and effective active phase interaction makes NCO-A a leading candidate for applications in battery technology.

In light of the fact that the electrode kinetics are linked to the capacitance of the electrode materials. Therefore, comprehensive examinations were conducted on the rapid and reversible electrochemical reactions of the NCO electrodes based on their CVs. Furthermore, the following relation was employed to evaluate the electrode materials' area-normalized capacitance (C_A).[45,46]

$$C = C_A A = \frac{\varepsilon_0 \varepsilon_r A}{d} \quad (4)$$

where C represents the specific capacitance (F g^{-1}), ε_r is the relative dielectric constant of the electrolyte (for H_2O: 80.1), ε_0 stands for the dielectric constant in a vacuum, A denotes the exposed area of the electrode to the electrolyte (m^2 g^{-1}), C_A refers to the electrode materials' area-normalized capacitance (F m^{-2}), and d represents the distance of charge separation (~1 nm). The analysis revealed that the NCO-A electrode material displayed a higher C_A value of 73 mF cm^{-2} compared to the other electrodes (Fig. 3a). Specifically, NCO-B exhibited a C_A of ~42 mF cm^{-2}, NCO-C revealed a C_A of ~38 mF cm^{-2}, and NCO-D showed a C_A of ~30 mF cm^{-2}. These results provide further support for the notion that not only do the properties of the electrode materials play a critical role but also the surface area of the electrode itself. This emphasizes the importance of considering the synergetic effect of both the electrode materials and their surface area in electrochemical processes. In addition, to support the evidence above, the surface concentration (Γ) of the electroactive site was calculated using Laviron's equation based on the CVs.[47,48]

$$\Gamma = \frac{Q}{nFA} \quad (5)$$

where Q denotes the charge (mC) determined from the oxidative peak area of the CV, A represents the electrode area (cm^2), n denotes the quantity of electrons engaged in the electrode reaction, and F stands for the Faraday constant. In the calculation, the estimated values indicated that the NCO-A electrode maintains a higher concentration of electroactive species on its surface (47.58×10^{-9} mol cm^{-1}) compared to the NCO-B, NCO-C, and NCO-D electrodes, which have concentrations of 43.19×10^{-9} mol cm^{-1}, 35.91×10^{-9} mol cm^{-1}, and 32.50×10^{-9} mol cm^{-1}, respectively (Fig. 3b). This suggests that NCO-A has a higher concentration of electroactive species, making it a promising candidate for further electrochemical studies. The evidence for this was substantiated by the peak current densities of the four electrodes, as indicated in the graphs of redox peak current (i) plotted against the square root of the sweep rate ($\sqrt{v}$) (refer to Fig. 3c and S15a–c†).[49] The anodic slopes exhibited the following descending order: NCO-A (7.31) > NCO-B (6.30) > NCO-C (5.70) > NCO-D (5.17). Meanwhile, the overall electrochemical energy stored in the electrode material results from the combination of charges that are controlled by both

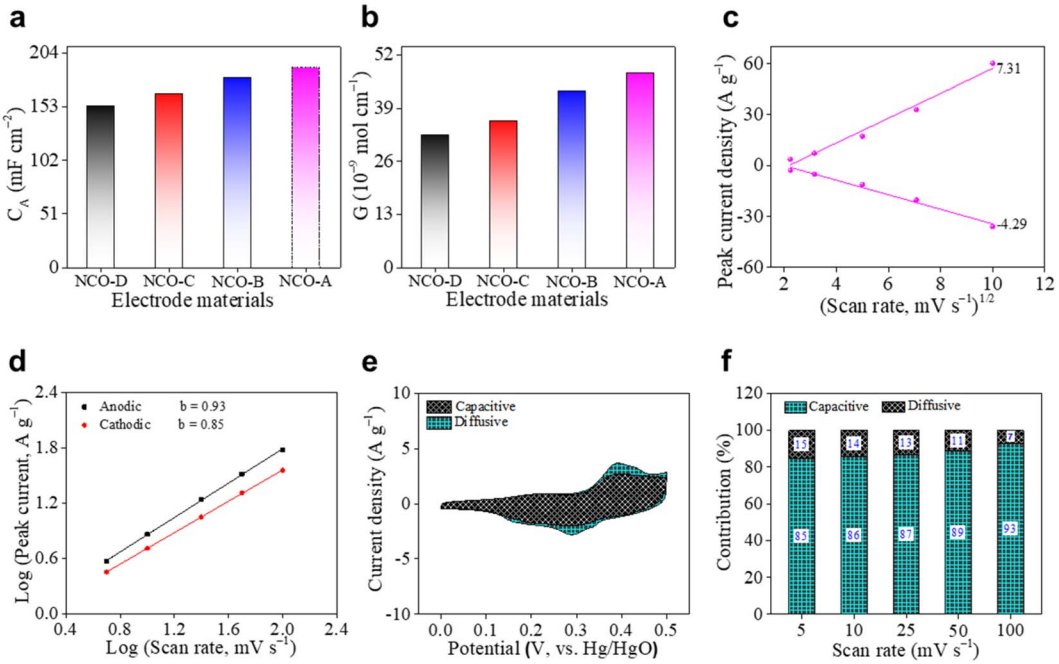

Fig. 3 (a) Comparison plot of area normalized capacitance (C_A): NCO-A, NCO-B, NCO-C, and NCO-D electrode materials; (b) histogram of surface concentration of the electroactive site (Γ): NCO-A, NCO-B, NCO-C, and NCO-D electrode materials; (c) peak current as a square root of scan rates for the NCO-A nanomaterial, (d) power law profile (log(I) *vs.* log(v)) at various sweep rates, (e) CV profiles of capacitive- and diffusive-controlled process, and (f) bar chart of surface- and diffusion-controlled contributions at different scan rates of the NCO-A electrode material.

diffusion and surface mechanisms. To ascertain the main charge storage kinetics of the hierarchical NCO-A nanostructure electrode, one can examine the correlation between the peak current i and applied sweep rate v, employing the power law to the CVs at varied scan rates. This approach provides a more comprehensive understanding of the electrode's electrochemical performance. The power law equation, which relates the peak current (i) to the adjustable parameter (a), the power law exponent (b), and the applied scan rate (v), can be mathematically expressed as $i = av^b$. Taking the logarithm of both sides of the equation yields the following expression:[22,50]

$$\log(i) = \log(a) + b \times \log(v) \quad (6)$$

Specifically, by plotting the logarithm of current (i) against the logarithm of frequency (v), the exact power exponent (b) associated with this relationship can be attained. The value of b can be calculated by determining the slope of the linear curves obtained from this plot, as demonstrated in Fig. 3d and S15d–f.† When the value of b is close to 1, it indicates that the material exhibits electrochemical behavior similar to a capacitive type. In contrast, when the b value is nearly 0.5, it signifies that the predominant behavior is diffusion-controlled charge storage kinetics. The oxidation and reduction peaks were analyzed to determine the b values, which were found to be ~0.93 and 0.85, respectively, through measurements of the redox peak current. The results indicate that the hierarchical NCO-A nanostructure electrode's facile faradaic battery-type process is primarily governed by its surface capacitive process characteristics, contributing to the overall stored charges.

Additionally, Dunn's approach was implemented to determine the proportion of capacitive and diffusive contributions to the overall capacitance of the electrodes. The following equations were employed to determine the aforementioned percentages:[22,50]

$$i = k_1 v + k_2 v^{1/2} \quad (7)$$

$$i/v^{1/2} = k_1 v^{1/2} + k_2 v \quad (8)$$

where k refers to a constant, while i represents the response current. The subscripts k_2v and k_1v indicate diffusion and capacitive-governed processes, respectively. By applying eqn (8), a linear plot was obtained by plotting $i/v^{1/2}$ *vs.* $v^{1/2}$. This allowed the calculation of k_1 and k_2 values from the intercept of the linear plots, which, in turn, were used to determine the contribution ratios of the diffusion- and capacitive-governed electrochemical properties, respectively, as presented in Fig. 3e. At a scan rate of 5 mV s^{-1}, the capacitive-dominant process contributed the most (85%), as it did at a scan rate of approximately 25 mV s^{-1} (87%). Furthermore, with an increase in the scan rate (around 100 mV s^{-1}), there was a gradual increase in the capacitive-governed process ratio, reaching a maximum of 93% (Fig. 3f). Furthermore, it can be observed that the faradaic redox behaviors exhibited by the battery-type electrode under surface capacitive control are more prevalent in all of the scan rate regions, strongly aligning with the previous observations made through CV (Fig. 2h). Thus, the

influence of surface capacitive kinetics plays a crucial role in improving the hierarchical NCO-A nanostructure electrode's rate behavior and energy storage performance to a higher degree.

To investigate the viable usage of the hierarchical porous sheet-like NCO-A nanoarchitecture, an HSC was fabricated using the hierarchical NCO-A nanostructure as the positive electrode, commercial AC (MSP20) as the negative electrode, and an aqueous solution of 6 M KOH as an electrolyte. The schematic illustration in Fig. 4a depicts the systematic evolution of the operational mechanisms involved in the fabrication of an HSC through the utilization of NCO-A and AC electrodes during the electrochemical energy storage process. The optimal mass ratio of the hierarchical NCO-A nanostructure positive and AC negative electrodes was determined to be ~0.81 to achieve superior electrochemical performance for the assembled NCO-A//AC HSC. In addition, the total weight loading of active materials was ~3.0 mg cm^{-2}. The hierarchical NCO-A nanostructure electrode has the ability to function within a positive working potential range of 0–0.5 V. On the other hand, the AC operates best in a negative range of −1.0–0 V, as demonstrated in Fig. S16a.† CV analysis of the AC electrode displayed the typical traits of EDLCs. It is necessary to carefully adjust the operating voltage window of the HSC to achieve high energy density while maintaining power density and cycling life despite adjusting the mass loading of the positive and negative electrodes. Otherwise, the electrolyte and electrode materials in a device begin to degrade, which can lead to undesired side reactions at the interface. This can harm the device's cycling performance and overall functionality. The CV profiles of the commercial AC were carefully analyzed over a range of scan rates, specifically between 10 and 100 mV s^{-1}. This analysis was conducted over a potential window of −1.0 to 0 V. The resulting CV curves exhibited a typical rectangular shape, which is characteristic of EDLCs, as depicted in Fig. S16b.† The consistency of the rectangular profile across different scan rates highlights the impressive electrochemical reversibility of the AC electrode. Such pronounced electrochemical reversibility is crucial, especially in the design and construction of HSCs. It ensures that the negative electrode can deliver reliable and efficient energy storage capabilities, which is essential for the overall performance and reliability of energy storage devices. Therefore, an optimization process was carried out to determine the operating voltage window of the NCO-A//AC-based HSCs. Fig. S16c† illustrates the CVs of the HSC across various voltage ranges (1.1 to 1.5 V) at 50 mV s^{-1}, indicating a robust operating voltage stability of up to 1.5 V without electrolyte decomposition. This finding confirms that the developed aqueous HSC is capable of supporting electronic devices with a maximum working voltage of 1.5 V. Furthermore, the CV analysis reveals distinct redox peaks, highlighting a dual capacitive mechanism that significantly contributes to the overall capacitance of the HSC. Additionally, GCD analysis was performed with varying cut-off voltage values ranging from 0–1.1 V to 0–1.5 V while maintaining a fixed current density of 5 A g^{-1}, as shown in Fig. S16d.† The GCD analysis presents the impressive capacitive

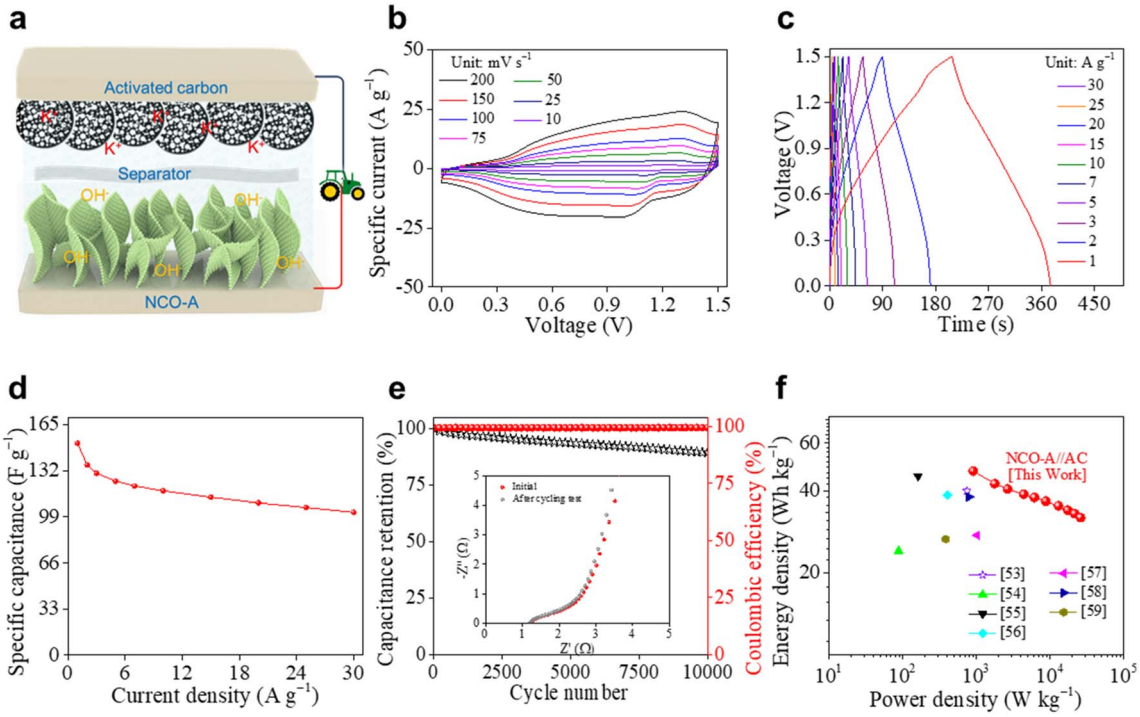

Fig. 4 Electrochemical performances of the HSC (NCO-A//AC): (a) a schematic illustration of two-electrode assembly-based HSCs using battery-type NCO-A as positive and commercial AC (MSP20) as negative electrodes, (b) CVs at different scan rates, (c) GCD profiles at different current densities, (d) plot of specific capacitance as a function of specific currents, (e) long-term cycling stability performance (the inset shows the Nyquist impedance plots before and after cycling), and (f) Ragone plot.

performance of the fabricated HSC. Furthermore, the HSC demonstrates quasi-symmetrical triangular GCD features even under high voltage windows of 1.5 V. The results of the study reveal their potential for energy storage applications. It is fascinating to observe that the GCD profiles demonstrate no noticeable IR drop. This could potentially indicate that the HSC under investigation is highly efficient and well-designed. This study confirms that the best operational voltage range for the HSC is 1.5 V, which results in excellent capacitive performance. The CVs of the optimized HSC at various scan rates ranging from 10 to 200 mV s^{-1} and over voltage windows spanning from 0 to 1.5 V are presented in Fig. 4b. The CV outcome of the HSC indicates the presence of both EDLC and faradaic redox characteristic peaks. These observations are attributed to the AC and hierarchical sheet-like NCO-A nanoarchitecture. The excellent redox behavior is evident in all the CVs. Even at a high sweep rate of 200 mV s^{-1}, the CVs' shape remains well-maintained, indicating that the HSC exhibits remarkable rate performance. Furthermore, it demonstrates that the NCO-A//AC HSC exhibits outstanding reversibility and rapid charge-transfer kinetics. The GCD profiles of the NCO-A//AC HSC are displayed in Fig. 4c. The profiles depict the HSC's performance at different current densities ranging from 1 to 30 A g^{-1} within an operating voltage window ranging from 0 to 1.5 V. The nonlinear GCD profiles serve as additional evidence to support the involvement of clear battery-type faradaic redox reactions, consistent with the results obtained from the CVs. The GCD profiles of the HSC displayed a high degree of symmetry, and even at a current density of 30 A g^{-1}, the IR drop is negligible, indicating the low internal resistance and excellent coulombic and energy efficiency of the HSC. Fig. 4d displays the specific capacitance of the HSC, which is determined from GCD profiles at various current densities ranging from 1 to 30 A g^{-1}. The NCO-A//AC HSC demonstrated exceptional performance by achieving a remarkable specific capacitance of 152 F g^{-1} at a current density of 1 A g^{-1}. This specific capacitance value is notably higher than reported recently for HSCs based on BTMOs.[43,51,52] The HSC device exhibited high rate capability, retaining 69.2% of its capacitance even at a high current density of 30 A g^{-1}. The cycling stability performance of the HSC device is another critical concern when evaluating the feasibility of the modern industrial sector. Furthermore, maintaining performance over numerous charge–discharge cycles is essential for a long-lasting and reliable device. Therefore, the NCO-A//AC HSC device was evaluated for cycling performance at a current density of 5 A g^{-1} with 10 000 consecutive charge–discharge cycles, as exhibited in Fig. 4e. The HSC device reveals an exceptional capacitance retention rate of 90.8% even after 10 000 cycles, which indicates its suitability for practical energy storage applications. Additionally, the HSC has a high coulombic efficiency of ~99.5%, as observed during the cycling performance tests. The excellent cycling stability could be attributed to the presence of an adequate amount of void space within the hierarchical sheet-like architecture of the NCO-A nanostructure, which helps to accommodate the changes in volume during cycling. The NCO-A//AC HSC device exhibits an exceptional cycling performance, outperforming other HSCs reported in the literature.[53,54] This remarkable stability is a promising characteristic for developing more reliable energy storage devices. The splendid cycling stability of the HSC device was further verified by performing EIS before and after the stability test, as depicted in the inset of Fig. 4e. Besides, the equivalent circuit was used to model the Nyquist plots, and the fit parameters are listed in Fig. S17 and Table ST2.† The impedance spectra reveal a low R_{ct} value of 0.457 Ω for the NCO-A//AC HSC, which marginally increases from ~0.457 to ~0.461 Ω after 10 000 GCD cycles. Moreover, the slope of the linear portion of the graph in the low-frequency range exhibited a high degree of similarity. However, a slight increase in Warburg resistance (6.11 to 8.06 Ω) might be due to minor degradation of the electrolytic components during prolonged charge/discharge cycles. These EIS results demonstrate the exceptional cycling stability of the NCO-A//AC HSC, with no noticeable loss or degradation of electrode materials throughout the testing period. Additionally, the HSC exhibits exceptional electrical conductivity, resulting in a remarkably low internal resistance. As a result, it exhibits outstanding electrochemical performance and durability. The energy and power densities play a crucial role in determining the feasibility of an HSC device in practical applications. These parameters are of fundamental importance in the field of energy storage and directly influence the performance and efficiency of the device. Therefore, the estimated outcomes are integrated into the Ragone plot of the NCO-A//AC HSC device, as shown in Fig. 4f. The high energy density of the fabricated HSC is noteworthy, with a recorded value of ~47.3 W h kg^{-1} at an operating power density of ~908.2 W kg^{-1}. Despite the increase in power density up to ~26.0 kW kg^{-1}, the NCO-A//AC HSC retains a respectable energy density of ~31.9 W h kg^{-1}. The NCO-A//AC HSC exhibits superior energy and power densities compared to the previously reported HSCs, as highlighted in Fig. 4f and Table ST3.†[53–59] The high electrochemical performance of the NCO-A//AC HSC is due to the distinctive morphology with a porous and layered sheet-like NCO-A void space nanoarchitecture, which provides a high surface area, excellent conductivity, and effective ion/electron transport. Following the completion of the rigorous long-term cycling tests, an in-depth examination of the morphology of the NCO-A electrode was conducted using *ex situ* SEM measurements at various magnifications. This detailed analysis was performed to assess the structural integrity and stability of the electrode material following extensive electrochemical cycling. The findings from this investigation are illustrated in Fig. S18.† The SEM images reveal that the electrode material maintains its distinct sheet-like nanoarchitecture, even after prolonged cycling under conditions that typically stress electrode materials. This retention of morphology is a significant indicator of the material's structural stability, suggesting that the underlying framework of the electrode remains intact throughout the entire testing period. Moreover, the remarkable endurance and consistent electrochemical performance exhibited by the NCO-A electrode across a multitude of cycles can be attributed to its strategic design that incorporates void spaces between the sheets. These voids play a crucial role during the electrochemical reactions as they effectively prevent the sheets from aggregating or

collapsing. This structural feature not only enhances the mechanical durability of the electrode but also facilitates optimal ionic transport, leading to sustained high performance even under continuous cycling conditions. The combination of these factors underscores the NCO-A electrode's potential for long-term application in energy-related technologies. Thus, the results of this work indicate that the NCO-A//AC HSC possesses the essential qualities to be considered a promising electrode material for advanced energy storage systems.

4. Conclusion

We present MOF-derived electrode nanoarchitectures for hybrid supercapacitors (HSCs), featuring nickel cobaltite nanosheets with a thickness of ~10–16 nm and extensive porous networks. The synthesis process utilizes MOF templates to create interconnected pores between nanoparticles. The resulting NCO layered nanosheets demonstrate exceptional performance as electrode materials, achieving a high specific capacity (~597 mA h g^{-1} at 1 A g^{-1}) and excellent rate capability. Notably, the HSC showcases a significant energy density (47.3 W h kg^{-1} at 908.2 W kg^{-1}) and remarkable cycle stability, maintaining performance over 10 000 cycles, surpassing state-of-the-art metal oxide-based supercapacitors. This work introduces a new method for advanced TMO electrodes, enhancing supercapacitor performance. Future research should refine synthesis and explore other metal-oxide materials to enhance energy storage technologies.

Data availability

The data supporting this article have been included as part of the ESI.†

Author contributions

Periyasamy Sivakumar: conceptualization, investigation, methodology, funding acquisition, data curation and interpretation, validation, writing – original draft. Jayaraman Balamurugan: validation, writing – review & editing. C. Justin Raj: methodology, writing – review & editing. Palaniappan Subramanian: validation, writing – review & editing. Antonysamy Dennyson Savariraj: formal analysis, writing – review & editing. Ramu Manikandan: validation, writing – review & editing. Hyun Jung: resources, funding acquisition, writing – review & editing.

Conflicts of interest

The authors declare that they have no known competing financial interests or personal relationships that could have appeared to influence the work reported in this paper.

Acknowledgements

This research was supported by the National Research Foundation of Korea (NRF), funded by the Korean government (MSIT) (No. NRF-2022R1F1A1063811) and (No. NRF-2022R1F1A1064008).

References

1 Z. Ahsan, Z. Cai, S. Wang, M. Moin, H. Wang, D. Liu, Y. Ma, G. Song and C. Wen, *Adv. Energy Mater.*, 2024, **14**, 2400373.
2 C. Xiong, Y. Zhang and Y. Ni, *J. Power Sources*, 2023, **560**, 232698.
3 S. Xu, Y. Li, T. Mo, G. Wei and Y. Yang, *Energy Storage Materials*, 2024, **69**, 103379.
4 M. Huang, J. Yu, H. Su, Z. Wu and Z. Li, *Appl. Surf. Sci.*, 2025, **681**, 161547.
5 N. Roy, G. Rajasekhara Reddy, M. R. Pallavolu, R. R. Nallapureddy, M. Dhananjaya, A. Sai Kumar, A. N. Banerjee, B.-K. Min, H. R. Barai and S. W. Joo, *ACS Appl. Mater. Interfaces*, 2024, **16**, 34859–34879.
6 J. Zhang, K. Wang, P. Lu, J. Gao, Z. Cao, F. Mo, D. Ho, B. Li and H. Hu, *Adv. Funct. Mater.*, 2024, **34**, 2310775.
7 Z. Li, J. Yu, C. Shi, H. Su and L. Bai, *J. Energy Storage*, 2024, **91**, 112082.
8 M. Girirajan, A. K. Bojarajan, I. N. Pulidindi, K. N. Hui and S. Sangaraju, *Coord. Chem. Rev.*, 2024, **518**, 216080.
9 Z. Li, C. Shi, J. Yu and L. Bai, *Appl. Surf. Sci.*, 2024, **669**, 160534.
10 H. Zhou, L. Guo, R. Zhang, L. Xie, Y. Qiu, G. Zhang, Z. Guo, B. Kong and F. Dang, *Adv. Funct. Mater.*, 2023, **33**, 2304154.
11 K. K. Haldar, R. Biswas, A. Arya, I. Ahmed, S. Tanwar and A. L. Sharma, *J. Energy Storage*, 2022, **4**, e378.
12 K. Xiang, D. Wu, Y. Fan, W. You, D. Zhang, J.-L. Luo and X.-Z. Fu, *Chem. Eng. J.*, 2021, **425**, 130583.
13 J. Yang, L. Ye, J. Sun, C. Li, X. Zhao, J. Liu and C. Sun, *J. Alloys Compd.*, 2023, **947**, 169694.
14 M. Sivakumar, B. Muthukutty, G. Panomsuwan, V. Veeramani, Z. Jiang and T. Maiyalagan, *Colloids Surf., A*, 2022, **648**, 129188.
15 Y. Jiang, F. Wu, Z. Ye, C. Li, Y. Zhang, L. Li, M. Xie and R. Chen, *Adv. Funct. Mater.*, 2021, **31**, 2009756.
16 I. Hussain, C. Lamiel, S. Sahoo, M. Ahmad, X. Chen, M. S. Javed, N. Qin, S. Gu, Y. Li, T. Nawaz, M. Z. Ansari and K. Zhang, *Mater. Today Phys.*, 2022, **27**, 100844.
17 S. Yuan, X. Duan, J. Liu, Y. Ye, F. Lv, T. Liu, Q. Wang and X. Zhang, *Energy Storage Materials*, 2021, **42**, 317–369.
18 R. Kumar, S. Sahoo, E. Joanni, R. K. Singh and R. M. Yadav, *Mater. Today Nano*, 2023, **24**, 100399.
19 P. Kumbhakar, C. C. Gowda, P. L. Mahapatra, M. Mukherjee, K. D. Malviya, M. Chaker, A. Chandra, B. Lahiri, P. M. Ajayan, D. Jariwala, A. Singh and C. S. Tiwary, *Mater. Today*, 2021, **45**, 142–168.
20 G. Cai, P. Yan, L. Zhang, H.-C. Zhou and H.-L. Jiang, *Chem. Rev.*, 2021, **121**, 12278–12326.
21 A. Dennyson Savariraj, C. Justin Raj, A. M. Kale and B. C. Kim, *Small*, 2023, **19**, 2207713.
22 Z. Abbas, N. Hussain, S. Kumar and S. M. Mobin, *Nanoscale*, 2024, **16**, 868–878.
23 N. Raza, T. Kumar, V. Singh and K.-H. Kim, *Coord. Chem. Rev.*, 2021, **430**, 213660.

24 S. Li, Y. Gao, N. Li, L. Ge, X. Bu and P. Feng, *Energy Environ. Sci.*, 2021, **14**, 1897–1927.
25 W. Du, Y. Zheng, X. Liu, J. Cheng, R. C. K. Reddy, A. Zeb, X. Lin and Y. Luo, *Chem. Eng. J.*, 2023, **451**, 138626.
26 M. Pathak, P. Mutadak, P. Mane, M. A. More, B. Chakraborty, D. J. Late and C. S. Rout, *Mater. Adv.*, 2021, **2**, 2658–2666.
27 A. D. Salunkhe, P. S. Pawar, P. K. Pagare, A. N. Kadam, P. K. Katkar and A. P. Torane, *J. Electroanal. Chem.*, 2023, **939**, 117475.
28 P. Cai, J. Zhao, X. Zhang, T. Zhang, G. Yin, S. Chen, C.-L. Dong, Y.-C. Huang, Y. Sun, D. Yang and B. Xing, *Appl. Catal. B Environ.*, 2022, **306**, 121091.
29 Y. Zhu, C. Cao, J. Zhang and X. Xu, *J. Mater. Chem. A*, 2015, **3**, 9556–9564.
30 S. Chen, D. Huang, D. Liu, H. Sun, W. Yan, J. Wang, M. Dong, X. Tong and W. Fan, *Appl. Catal. B Environ.*, 2021, **291**, 120065.
31 R. P. Antony, A. K. Satpati, K. Bhattacharyya and B. N. Jagatap, *Adv. Mater. Interfaces*, 2016, **3**, 1600632.
32 X. Zhao, Y. Fu, J. Wang, Y. Xu, J.-H. Tian and R. Yang, *Electrochim. Acta*, 2016, **201**, 172–178.
33 C. Li, J. Balamurugan, D. C. Nguyen, N. H. Kim and J. H. Lee, *ACS Appl. Mater. Interfaces*, 2020, **12**, 21505–21514.
34 C. Li, J. Balamurugan, N. H. Kim and J. H. Lee, *Adv. Energy Mater.*, 2018, **8**, 1702014.
35 D. J. Patil, D. B. Malavekar, V. C. Lokhande, P. P. Bagwade, S. D. Khot, T. Ji and C. D. Lokhande, *Energy Technol.*, 2022, **10**, 2200295.
36 S. R. Khaladkar, O. Maurya, G. Gund, B. Sinha, D. Dubal, R. Deshmukh and A. Kalekar, *ACS Appl. Mater. Interfaces*, 2024, **16**, 11408–11420.
37 S. R. Khaladkar, O. Maurya, G. Gund, B. Sinha, D. Dubal, R. R. Deshmukh and A. Kalekar, *J. Energy Chem.*, 2023, **87**, 304–313.
38 R. R. Deshmukh and A. R. Shetty, *J. Appl. Polym. Sci.*, 2008, **107**, 3707–3717.
39 K.-Y. Law, *Pure Appl. Chem.*, 2015, **87**, 759–765.
40 J. Yu, D. Yao, Z. Wu, G. Li, J. Song, H. Shen, X. Yang, W. Lei, F. Wu and Q. Hao, *ACS Appl. Energy Mater.*, 2021, **4**, 3093–3100.
41 G.-T. Xiang, N. Chen, B. Lu, J.-L. Xu, R. D. Rodriguez, E. Sheremet, Y.-D. Hu and J.-J. Chen, *Nano Energy*, 2023, **118**, 108936.
42 L. Han, J. Luo, R. Zhang, W. Gong, L. Chen, F. Liu, Y. Ling, Y. Dong, Z. Yong, Y. Zhang, L. Wei, X. Zhang, Q. Zhang and Q. Li, *ACS Nano*, 2022, **16**, 14951–14962.
43 O. R. Ankinapalli, B. N. V. Krishna and J. S. Yu, *J. Power Sources*, 2024, **591**, 233877.
44 P. Siva and K. Vasu, *J. Mater. Chem. A*, 2024, **12**, 961–967.
45 R. Kötz and M. Carlen, *Electrochim. Acta*, 2000, **45**, 2483–2498.
46 H. Ji, X. Zhao, Z. Qiao, J. Jung, Y. Zhu, Y. Lu, L. L. Zhang, A. H. MacDonald and R. S. Ruoff, *Nat. Commun.*, 2014, **5**, 3317.
47 E. Laviron, *J. Electroanal. Chem. Interfacial Electrochem.*, 1979, **101**, 19–28.
48 Y. Yin, G. Huang, M. Di, C. Xue, W. Li, L. Zhang and Y. Liu, *Res. Chem. Intermed.*, 2017, **43**, 873–883.
49 G. Nagaraju, S. C. Sekhar, B. Ramulu, Sk. K. Hussain, D. Narsimulu and J. S. Yu, *Nano-Micro Lett.*, 2020, **13**, 17.
50 J. Yu, H. Su, C. Shi, G. Qiu, L. Bai and Z. Li, *Electrochim. Acta*, 2023, **471**, 143392.
51 A. Rashti, X. Lu, A. Dobson, E. Hassani, F. Feyzbar-Khalkhali-Nejad, K. He and T.-S. Oh, *ACS Appl. Energy Mater.*, 2021, **4**, 1537–1547.
52 Y. Wu, Z. Zhang, W. Liu, Y. Zheng, J. Su, L. Li, N. Liu and Y. Gao, *J. Power Sources*, 2022, **520**, 230816.
53 P. M. Shafi, D. Mohapatra, V. P. Reddy, G. Dhakal, D. R. Kumar, D. Tuma, T. Brousse and J.-J. Shim, *Energy Storage Materials*, 2022, **45**, 119–129.
54 R. Abazari, S. Sanati, A. Morsali and D. P. Dubal, *J. Mater. Chem. A*, 2021, **9**, 11001–11012.
55 B. Yin, L. Hao, T. Wei, C. Wang, B. Zhu, X. Li and Q. Yang, *J. Power Sources*, 2022, **533**, 231409.
56 W. Li, W. Zhang, S. Hao and H. Wu, *Langmuir*, 2023, **39**, 12510–12519.
57 B. Shen, X. Liao, X. Hu, H.-T. Ren, J.-H. Lin, C.-W. Lou and T.-T. Li, *J. Mater. Chem. A*, 2023, **11**, 16823–16837.
58 Y. Sun, S. Liu, N. Huang, X. Wang, J. Liu, J. Bi, J. Zhang, L. Guo and X. Sun, *J. Power Sources*, 2022, **545**, 231911.
59 B. N. V. Krishna, S. K. Hussain and J. S. Yu, *J. Power Sources*, 2021, **506**, 230193.